

<https://doi.org/10.1038/s43247-024-01981-9>

Projected changes in African easterly wave activity due to climate change

Check for updates

Akintomide A. Akinsanola^{1,2}✉, Adeyemi A. Adebisi³, Vishal Bobde¹, Oluwafemi E. Adeyeri^{4,5}, Alain T. Tamoffo⁶ & Derrick K. Danso⁷

African easterly waves significantly influence regional hydroclimate, making it crucial to understand how global warming will impact their activity. Here, we investigate future changes in wave activity and assess the underlying mechanisms using an ensemble of Earth system models. We find a robust increase in wave activity over the Sahel–Sahara region by the end of the 21st century under two emission scenarios. This intensification is linked to increased baroclinicity associated with a strengthening of the meridional temperature gradient between the Guinea Coast and the Sahara. Our results also indicate that low-level warming enhances the waves by reinforcing monsoon flow, leading to increased convergence and vertical motion along the intertropical discontinuity. These energetic alterations significantly modify the conditions that currently produce these waves. Overall, our findings suggest that changes in wave activity could impact the transport of Saharan dust and mesoscale convective activity over the Sahel.

African easterly waves (AEWs) are westward-propagating synoptic-scale disturbances that originate from central North Africa during boreal summer^{1,2}. These waves develop and propagate along the African Easterly Jet (AEJ)^{1,3,4}. Previous studies have linked AEW formation to the AEJ's combined barotropic-baroclinic instability, characterized by a reversal in the meridional gradient of potential vorticity (PV)^{1,3,5,6} as well as pre-existing convection over East Africa^{7,8}. Latent heating from moist convection and the radiative effects of Saharan dust also contribute to AEW growth and maintenance^{9–15}. Given the significant influence of AEWs on regional and global weather patterns—such as organizing mesoscale convective systems (MCSs), modulating Sahel rainfall, mobilizing Saharan dust, and acting as precursors for Atlantic tropical cyclone (TC) development^{1,7,8,12,16–23}—understanding how AEW characteristics (e.g., tracks) will change in a warmer future climate is crucial.

Previous studies have classified AEWs into two distinct types based on their periodicity: 3–5-day AEWs, which have wavelengths of 3000–5000 km with phase speeds of 8–12 m s⁻¹, and 6–9-day AEWs, which have longer wavelengths of 5000–6000 km and slower phase speeds of around 7 m s⁻¹^{1,2,8,16,24–31}. The 3–5-day AEWs follow two main tracks over West Africa: one near 5°N and the other around 15°N, merging over the tropical Atlantic at about 17.5°N. In contrast, 6–9-day AEWs are located north of the AEJ, near 17.5°N, over both West Africa and the

tropical Atlantic²⁸. Although the northern and southern AEW tracks are distinct, they often represent different phases of the same wave^{4,17,32}, and their impacts on regional and global climate vary. The southern track, which propagates near the Intertropical Convergence Zone (ITCZ), is typically associated with moist convection, has a greater influence on precipitation variability in West Africa, and is more efficient at undergoing tropical cyclogenesis^{16,25,33,34}. Conversely, the northern track, located within the near-surface baroclinic zone, is characterized by dry convective processes³⁵. These too can influence precipitation variability in the Sahel through the advection of moisture within the southerly flow of the vortex³⁵, but they are less efficient at undergoing tropical cyclogenesis^{33,36}. Additionally, since their track is near the southern edge of the Sahara, they play a crucial role in dust mobilization and transport across West Africa and the Atlantic³⁷. In many cases, the northern and southern tracks of an AEW often merge to form a single structure, typically over the Atlantic Ocean^{38,39}. These single-structured AEWs are often associated with the formation of TCs in the eastern Atlantic Ocean, contributing to more than half of such events⁴⁰.

Previous studies have examined the impact of climate change on AEWs using global^{33,41–43} and regional^{44,45} climate model simulations. For example, using simulations from the fifth phase of the Coupled Model Intercomparison Project (CMIP5), Skinner and Diffenbaugh³³ and Brannan and Martin⁴³

¹Department of Earth and Environmental Sciences, University of Illinois Chicago, Chicago, IL, USA. ²Environmental Science Division, Argonne National Laboratory, Lemont, IL, USA. ³Department of Life and Environmental Sciences, University of California–Merced, Merced, CA, USA. ⁴Low-Carbon and Climate Impact Research Centre, School of Energy and Environment, City University of Hong Kong, Kowloon, Hong Kong. ⁵Fenner School of Environment and Society, Australian National University, Canberra, ACT, Australia. ⁶Climate Service Center Germany (GERICS), Helmholtz-Zentrum Hereon, Hamburg, Germany. ⁷Department of the Earth, Atmosphere and Climate, Iowa State University, Ames, USA. ✉e-mail: aakinsan@uic.edu

reported a projected increase in the frequency and intensity of northern-track AEWs, whereas southern-track AEWs did not exhibit a robust response by the end of the twenty-first century. Similarly, Hannah and Aiyyer⁴², using a super-parameterized earth system model, found increased northern-track AEW activity due to enhanced baroclinicity and decreased southern-track activity, attributed to weakened temperature gradients. Martin and Thorncroft⁴¹ used CMIP5 and also observed reduced AEW activity in late spring and early summer but higher intensity from July to October, with southern-track responses being more uncertain due to poor model resolution of the Guinea Highlands. In contrast, Kebe et al.⁴⁴, using a regional climate model (RCM, at 25 km resolution), projected a future decrease in AEW activity due to decreased barotropic and baroclinic instability. Additionally, they reported a strengthened and southward-shifted AEJ, attributed to a shift in the meridional temperature gradient (MTG). However, Bercos-Hickey and Patricola⁴⁵ found a projected increase in AEW frequency and intensity using another RCM. These varying results highlight significant uncertainty in the future behavior of AEWs, likely due to differences in model physics, resolution, tracking methods, and climate scenarios.

Studies have documented significant improvements in climate models' ability to capture key features of past and future climates, as seen in the progression from CMIP3 to CMIP5^{46,47}. The recent transition to CMIP6⁴⁸ includes updates such as better representation of physical processes, higher resolution, expansion of complexity by transitioning from General Circulation Models to Earth System Models, and new emission scenarios for future projections (i.e., shared socioeconomic pathways; SSP). However, it is unclear whether these updates will enhance the simulation of AEW activity and strengthen the reliability of projected changes. Therefore, this study builds on previous studies to investigate the future response of AEWs to global warming by leveraging CMIP6 simulations to address the following questions: (a) How well do CMIP6 models represent the characteristics of AEWs and their associated mechanisms? (b) How will AEW activity change in the future; will lower and higher emission scenarios lead to consistent or different results? (c) What are the dynamic and thermodynamic environments responsible for changes in AEW activity? A better understanding of AEW responses to global warming will provide valuable insights into the hydroclimate of West Africa and the broader Atlantic basin.

Results

Representation of AEW activity in CMIP6 present-day simulations

Realistic representation of the present-day climate is the basis for developing credible projections of future changes in global warming scenarios^{49,50}. Following previous studies^{33,41,51–54}, we use both the meridional wind variance (MWV) and eddy kinetic energy (EKE) approaches as proxies for AEW activity. These proxies are calculated for the 3–5-day and 6–9-day AEWs and are computed at 850 and 700 hPa to assess low- and mid-level AEW activity. First, we employ various descriptive statistical measures, including percentage bias, normalized root mean square error (NRMSE), pattern correlation coefficient (PCC), and Taylor skill score (TSS), to evaluate the accuracy of simulated AEW activity relative to ERA5. The results are presented in Figs. S1–S2 of the supplementary information. Generally, a low percentage bias and NRMSE, along with high PCC and TSS, are desirable.

For both the MWV and EKE approaches at 850 and 700 hPa, most CMIP6 models used here exhibit a high PCC (~0.9) and TSS (~0.7) for both the 3–5-day and 6–9 day-AEWs, with the exception of BCC-CSM2-MR, FGOALS-g3, and MIROC6, which show lower PCC (~0.6) and TSS (~0.5). For the 3–5-day AEWs (Fig. S1), five CMIP6 models (ACCESS-EM2, EC-Earth3, EC-Earth-CC, EC-Earth-Veg, and FGOALS-g3) considerably underestimate AEW activity, with percentage biases reaching ~–50%. In contrast, BCC-CSM2-MR exhibits the highest positive percentage biases (~25%). Other models show moderate biases, aligning more closely with ERA5. NRMSE values are consistent across all models for both metrics and pressure levels. NRMSEs remain considerably low for all models (<0.5) except for FGOALS-g3 across all metrics and levels, and ACCESS-EM2, EC-

Earth3, EC-Earth-CC, and EC-Earth-Veg for the MWV method at 850 hPa, where NRMSE exceeds 0.9. For the 6–9-day AEWs (Fig. S2), most CMIP6 models display a low percentage bias (<10%), except for BCC-CSM2-MR and CanESM5 (FGOALS-g3), which exhibit a positive (negative) bias of more than 20%. Only FGOALS-g3 has NRMSE >0.9, while other models generally exhibit values <0.5.

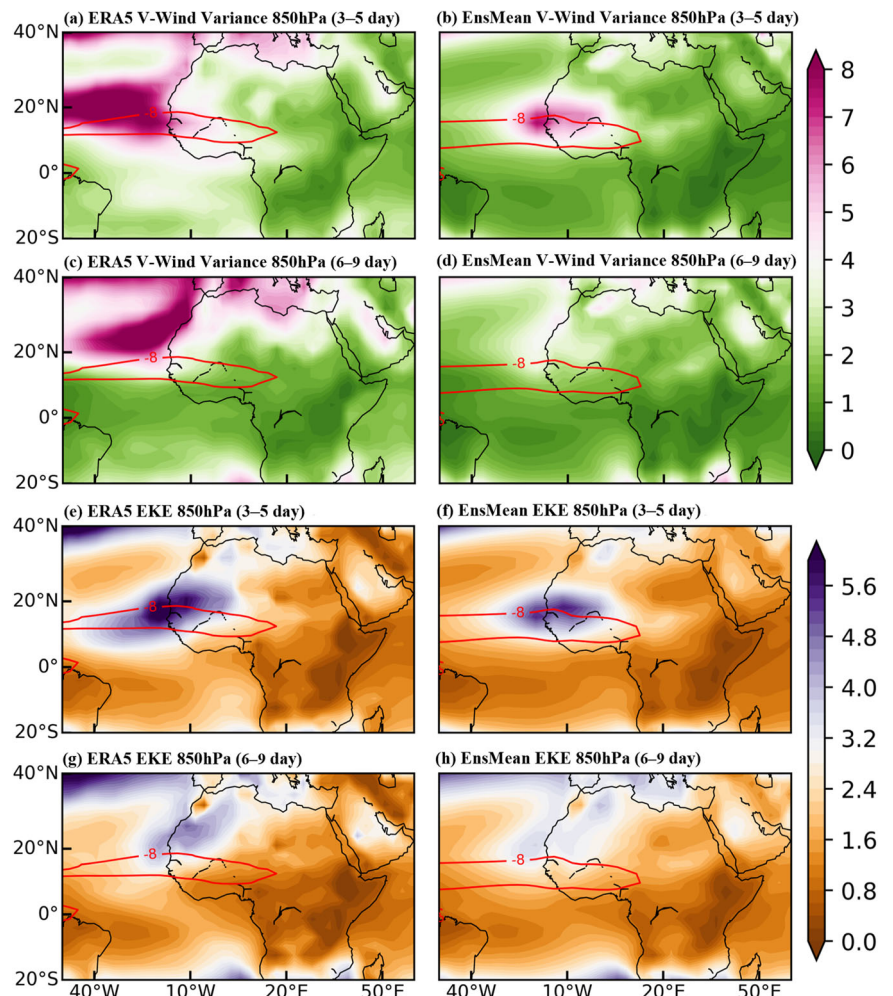
Figs. S3–S10 provide a clearer depiction of the variation in the representation of AEW activity by the CMIP6 models, in terms of both MWV (Figs. S3–S6) and EKE (Figs. S7–S10), both of which are spatially consistent. For instance, in the representation of the 3–5-day AEWs, some models (e.g., BCC-CSM2-MR and CanESM5) show higher magnitudes of AEW activity at both 850 hPa and 700 hPa compared to ERA5, while others (e.g., ACCESS-CM2 and FGOALS-g3) display relatively lower magnitudes. Overall, the largest biases relative to ERA5 occur mostly over land at the lower level and over the ocean at mid-level. We note that the biases reported herein have been a long-standing problem of global climate models^{33,41} and have not been significantly alleviated in CMIP6 models. Nevertheless, most of the models used in this study reasonably capture AEW activity.

Given that previous studies^{50,55} have noted that the multimodel ensemble mean (EnsMean) tends to reduce systematic biases in individual models by canceling out spatial errors, we further evaluate the performance of the CMIP6 EnsMean in accurately simulating the spatial distribution of present-day AEW activity. This assessment is made by comparing the results to ERA5 (Fig. 1 for 850 hPa and Fig. S11 for 700 hPa). Relative to ERA5, EnsMean considerably reproduces the present-day spatial distribution of both MWV and EKE for the 3–5-day and 6–9-day AEWs at both 850 hPa and 700 hPa. In the ERA5 reanalysis (Fig. 1a, c, e, g), the tracks of the 3–5-day (6–9-day) AEWs are evident at 850 hPa between 10°N and 25°N (15°N and 35°N) and west of 15°W and at the same latitudes at 700 hPa (Fig. S11a, c, e, g). EnsMean reasonably captures the location of maximum MWV and EKE, albeit with a lower magnitude (Figs. 1b, d, f, h and S11b, d, f, h). Our analysis shows a clear distinction between 3–5-day and 6–9-day AEW tracks at both 850 and 700 hPa in many CMIP6 models (Figs. S3–S10) and EnsMean (Figs. 1 and S11). Previous studies²⁸ demonstrated that 3–5-day AEWs typically follow two distinct tracks, one near 5°N and the other near 15°N, merging around 17.5°N over the tropical Atlantic. However, our analysis reveals that many CMIP6 models and EnsMean do not show a clear separation between these northern and southern tracks. This lack of distinction also noted in CMIP5 studies³³, is often attributed to coarse model resolution or an overestimated connection between AEW circulation and convection, leading to excessively strong AEW activity within the ITCZ over West Africa. Nevertheless, our results suggest the presence of vertically deeper AEWs in the Sahel and the Guinea Coast in West Africa, considering that some CMIP6 models accurately simulate the AEW activity north and south of the AEJ. Despite the noticeable biases, which could potentially impact future projections, the CMIP6 EnsMean reasonably reproduces the spatial distribution of AEW activity. Thus, a discussion based on EnsMean is credible.

Projected changes in AEW activity

We examine the potential changes in AEW activity by the end of the 21st century (Figs. 2 and S12 for EnsMean changes at 850 hPa and 700 hPa, respectively). The projected changes in individual models are presented in Figs. S13–S20 (Figs. S21–S28) based on MWV (EKE). Under future warming, there is strong intermodel agreement among the CMIP6 models that AEWs along the Sahel-Sahara border (~20°N) will intensify. This projected change is robust, as at least 70% of the models agree on the sign of EnsMean change across most grid points (see hatching on the figures). For 3–5-day AEWs, the zone of maximum change at 850 hPa (Fig. 2a, c, e, g) is between 12°N and 26°N and 20°E and 30°W for SSP5–8.5, and between 16°N and 25°N and 5°E and 25°W for SSP2–4.5. In this region, EnsMean shows an average increase of up to 0.9 m²s^{–2} under SSP2–4.5 and more than 1.5 m²s^{–2} under SSP5–8.5 in the JJAS mean MWV (Fig. 2a, c) and EKE (Fig. 2e, g). Similar projected increases in MWV and EKE are observed in nearly the same region at 700 hPa (Fig. S12), although the region of robust

Fig. 1 | Mean distribution of present-day African Easterly Wave activity. a–d JJAS mean meridional wind variability (shaded, m^2s^{-2}) and **e–h** JJAS mean EKE (shaded, m^2s^{-2}) at 850 hPa for 3–5-day (a, b, e, f) and 6–9-day (c, d, g, h) AEWs for the period 1985–2014. Mean averaged from ERA5 reanalysis (a, c, e, g) and CMIP6 EnsMean (b, d, f, h). The red contour line in a–h represents the $-8 ms^{-1}$ zonal wind contour at 700 hPa during 1985–2014, from ERA5 and the CMIP6 EnsMean, indicating the location of the AEJ core.



projected increase extends southward to the Guinea Coast of West Africa (near 2°N) under SSP5–8.5 (Fig. S12c, g). We note that eight CMIP6 models, mostly from the same institution (EC-Earth3-CC, EC-Earth3, EC-Earth3-Veg, MIROC6, MPI-ESM1-2-HR, MPI-ESM1-2-LR, NESM3, NorESM3-LM), contribute to the southward increase in AEW activity evident in EnsMean (Figs. S18 and S26). This may be attributed to model interdependence, where models developed by the same or closely collaborating institutions tend to share similar physics and parameterization schemes^{56–58}. Such interdependence can skew EnsMean; thus, caution is needed when interpreting such results, as the apparent consensus may not reflect independent lines of evidence but rather the overlap in model designs. Although model interdependence suggests a need for caution, the findings herein are robust and offer valuable insights into future AEW activity. Consistent with 3–5-day AEWs, we also find an intensification of 6–9-day AEWs (Figs. 2b, d, f, h and S12b, d, f, h), though the magnitude is 2–3 times lower, and the region of robust increase is confined mostly to land.

With the exception of SSP5–8.5 at 700 hPa, where the projected increase in 3–5-day AEWs by EnsMean extends to the Guinea Coast, the zone of enhanced AEW activity generally lies within and north of the maximum AEW activity observed during the present-day period (1985–2014) and projected future (2070–2099) location of the AEJ core. In general, at both 700 hPa and 850 hPa (except for 3–5-day AEWs at 700 hPa under SSP5–8.5), we find no robust changes in the EnsMean-projected AEW activity south of 12°N toward the Guinea Coast (i.e., on the cyclonic shear side of the AEJ). Previous studies³³ have noted that AEW activity south of 12°N is likely complicated by the response of moist convective processes to enhanced greenhouse forcing. Indeed, considerable variations exist across

individual models in the southern region. For instance, BCC-CSM2-MR and CESM2-WACCM project a future decrease in AEW activity across all levels and scenarios, while models such as EC-Earth3-CC, EC-Earth3, EC-Earth3-Veg, IPSL-CM6A-LR, MIROC6, MPI-ESM1-2-HR, MPI-ESM1-2-LR, and NESM3 (Figs. S13–S28) generally simulate future increases that extend to the Guinea Coast (i.e., south of 12°N). The inconsistency in the sign of projected changes in AEW activity south of 12°N (south of the AEJ) at 850 hPa and 700 hPa indicates higher uncertainty, and perhaps a lower likelihood of significant changes in AEW activity across the Guinea Coast of West Africa.

The relatively high-latitude location of the zone of maximum and robust increase in AEW activity (i.e., 12°N to 26°N) may suggest an influence from increased midlatitude trough activity^{59,60}. To further assess this, we examine the changes in midlatitude troughs and their potential contribution to changes in AEW activity. Following Chang et al.⁶¹, we use MWV at 250 hPa as a proxy for midlatitude storm track activity. Our results indicate that future changes in midlatitude trough activity have minimal impact on the robust changes in AEW activity (Figs. 3 and S29). Specifically, under both the SSP2–4.5 and SSP5–8.5 scenarios, we find a projected decrease in summer mean variability of 3–5-day (Fig. 3) and 6–9-day (Fig. S29) AEWs at 250 hPa north of 30°N but south of 60°N, covering large parts of southern Europe and the subtropical Atlantic (Figs. 3a, c and S29a, c). In contrast, a robust increase is evident north of 60°N, suggesting that the mean location of midlatitude troughs may shift northward under global warming. A similar pattern of robust changes in MWV is observed at 850 hPa between 30°N and 60°N (Figs. 3b, d and S29b, d). However, these changes are generally weaker, with a maximum variance of $-2.0 m^2s^{-2}$ at 850 hPa compared to more than

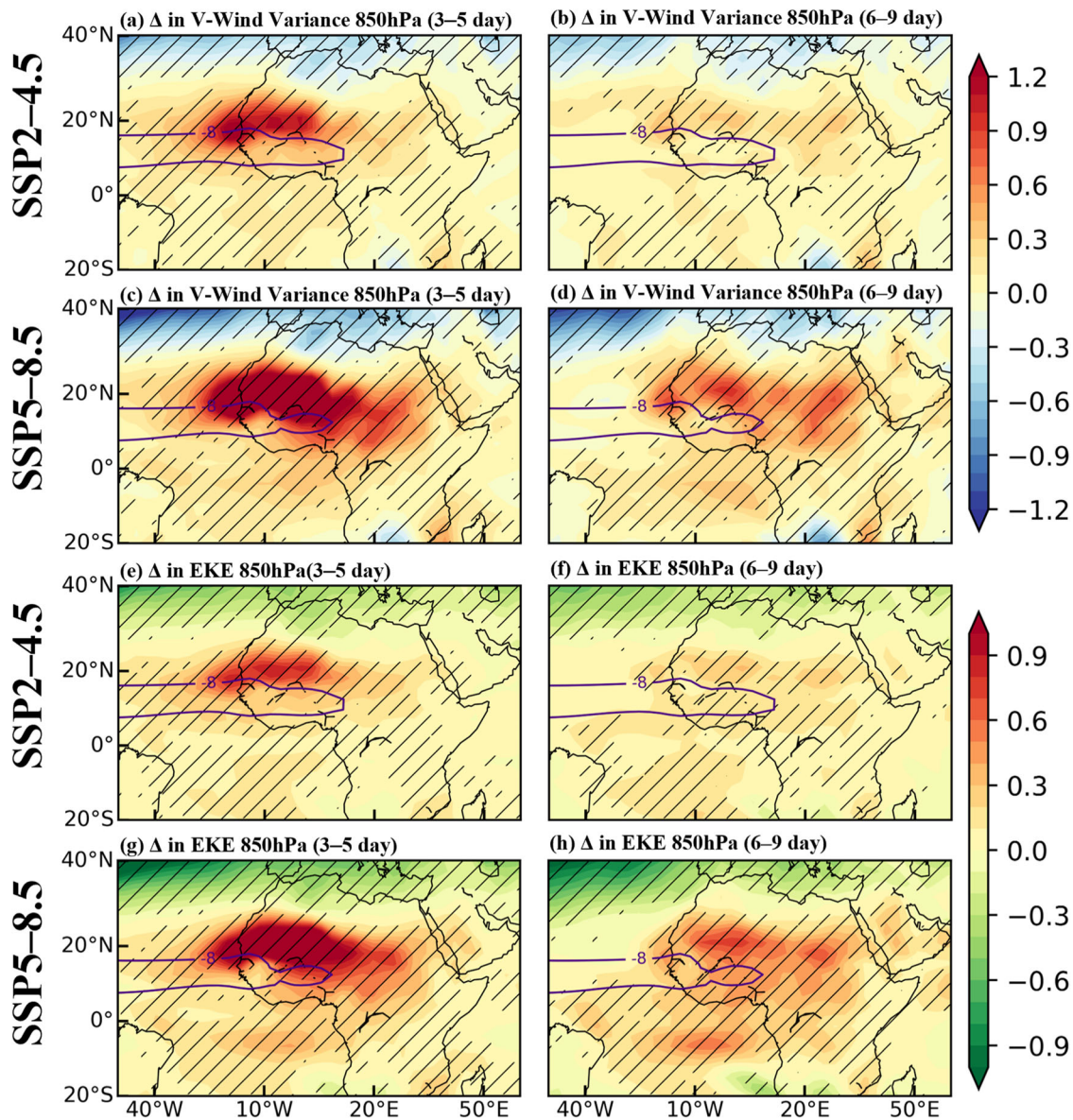


Fig. 2 | Projected changes in African Easterly Wave activity. a–d CMIP6 EnsMean change in JJAS meridional wind variability (shaded, m^2s^{-2}) and e–h CMIP6 EnsMean change in JJAS EKE (shaded, m^2s^{-2}) at 850 hPa for 3–5-day (a, c, e, g) and 6–9-day (b, d, f, h) AEWs under (a, b, e, f) SSP2–4.5 and (c, d, g, h) SSP5–8.5. Mean change calculated between 2070–2099 and 1985–2014. The purple contour in each plot

marks the -8 ms^{-2} zonal wind contour at 700 hPa during 2070–2099 and indicates the future location of the AEJ core. Hatching indicates grid points where at least 70% of ensemble members agree on the sign of the change in EnsMean.

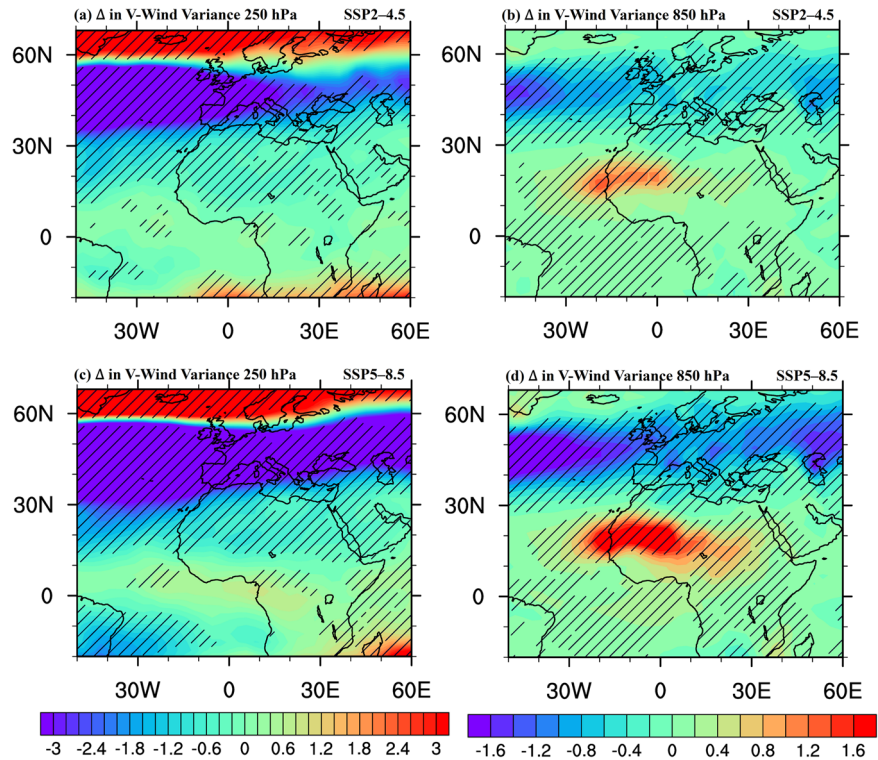
$-3.0\text{ m}^2\text{s}^{-2}$ at 250 hPa. Based on these findings, we conclude that changes in AEW activity drive most of the increased variability in MWV evident in the CMIP6 models. Similar results are found for EKE (Figure not shown).

Dynamic and thermodynamic factors contributing to future changes in AEW activity

Here, we assess the factors contributing to changes in AEW activity (i.e., EKE) by examining future changes in the underlying mechanisms. We first diagnose the Lorenz energy cycle⁶² and assess key energy conversion terms, including baroclinic energy and barotropic energy conversion, as well as diabatic heating. The primary energy source for eddies is available potential energy, which is converted into kinetic energy⁶². Both available potential energy and kinetic energy can be separated into their mean and eddy parts. Previous studies have shown that the northern-track AEWs, particularly along the Sahel-Sahara border (where this study identifies a higher likelihood of future changes), derive most of their energy from baroclinic

processes. These processes are associated with the interaction of low-level MTG in the Sahel-Sahara region and potential vorticity gradients within the AEJ core. Projected AEW energetics are expected to partially reflect local surface air temperature changes due to increased radiative forcing. Enhanced potential temperature gradients lead to increased zonal available potential energy (ZAPE), fueling AEW development^{33,35,63,64}. AEWs harness this reservoir of ZAPE by transferring temperature along the MTG and generating eddy available potential energy (EAPE). AEWs then grow by converting EAPE into EKE via baroclinic overturning. This continuous growth requires replenishing EAPE from the ZAPE reservoir⁶³. Figures 4a, b and S30a, b show the EnsMean meridional cross-section of the baroclinic energy conversion term ($-\frac{R}{p}\omega'T'$) for 3–5-day and 6–9-day AEWs under SSP5–8.5 and SSP2–4.5, respectively. For the 3–5-day AEWs, two distinct centers of positive baroclinic conversion values are evident in present-day simulations over West Africa (see contour line). The first is between 10°N and 22°N in the lower troposphere, spanning from the surface

Fig. 3 | Projected changes in African Easterly Wave activity. CMIP6 EnsMean change in JJAS meridional wind variability (shaded, m^2s^{-2}) for 3–5-day AEWs at 250 hPa (a, c) and 850 hPa (b, d) under SSP2–4.5 (a, b) and SSP5–8.5 (c, d). Mean change calculated between 2070–2099 and 1985–2014 (shaded, m^2s^{-2}). Hatching indicates grid points where at least 70% of ensemble members agree on the sign of the change in EnsMean.



to 650 hPa. This center is closely associated with either the ascent of warm air or the descent of cold air, most coinciding with the Saharan heat-low region⁶⁵. The second center is between 500 and 200 hPa from 0° to 16°N and is linked to latent heat release from AEW-induced convection, which drives the ascent of warm air at these levels. Similar regions of positive baroclinic energy conversion appear in the 6–9-day AEWs, though with reduced intensity compared to the 3–5-day AEWs. The pronounced baroclinic conversion in the upper troposphere for 3–5-day AEWs can be attributed to more intense convection, as simulated by the CMIP6 models. Under future warming (shading in Figs. 4a, b and S30a, b), both 3–5-day and 6–9-day AEWs show an increase in baroclinic energy conversion in both the lower and upper troposphere, although the 6–9-day waves remain less intense, consistent with their present-day patterns.

Our results consistently indicate that the projected conversion of ZAPE to EAPE is linked to future AEW development, as represented by negative t-v covariance (Fig. 5a, d) and negative meridional temperature gradient (MTG)-v covariance (Fig. S32). This conversion is intensified by the enhanced regional poleward MTG (Fig. S33). Notably, EnsMean reasonably reproduces the region of negative mean covariance of the filtered meridional wind and temperature over West Africa during the historical period (Fig. S31). Interestingly, both t-v covariance and MTG-v covariance become more negative in regions projected to experience increased AEW activity by the end of the 21st century, indicating a stronger temperature flux down the temperature gradient and greater EAPE for AEW growth (Figs. 5a, d and S32). Indeed, the MTG is projected to increase from the surface to the mid-troposphere (400 hPa), with the most significant increases occurring below 700 hPa over the Sahel-Sahara region, particularly between 14°N and 26°N (Fig. S33). The projected intensification of the MTG is likely to have a substantial impact on the zonal atmospheric circulation patterns through the thermal wind relationship^{66,67}, subsequently affecting the future position and strength of the AEJ.

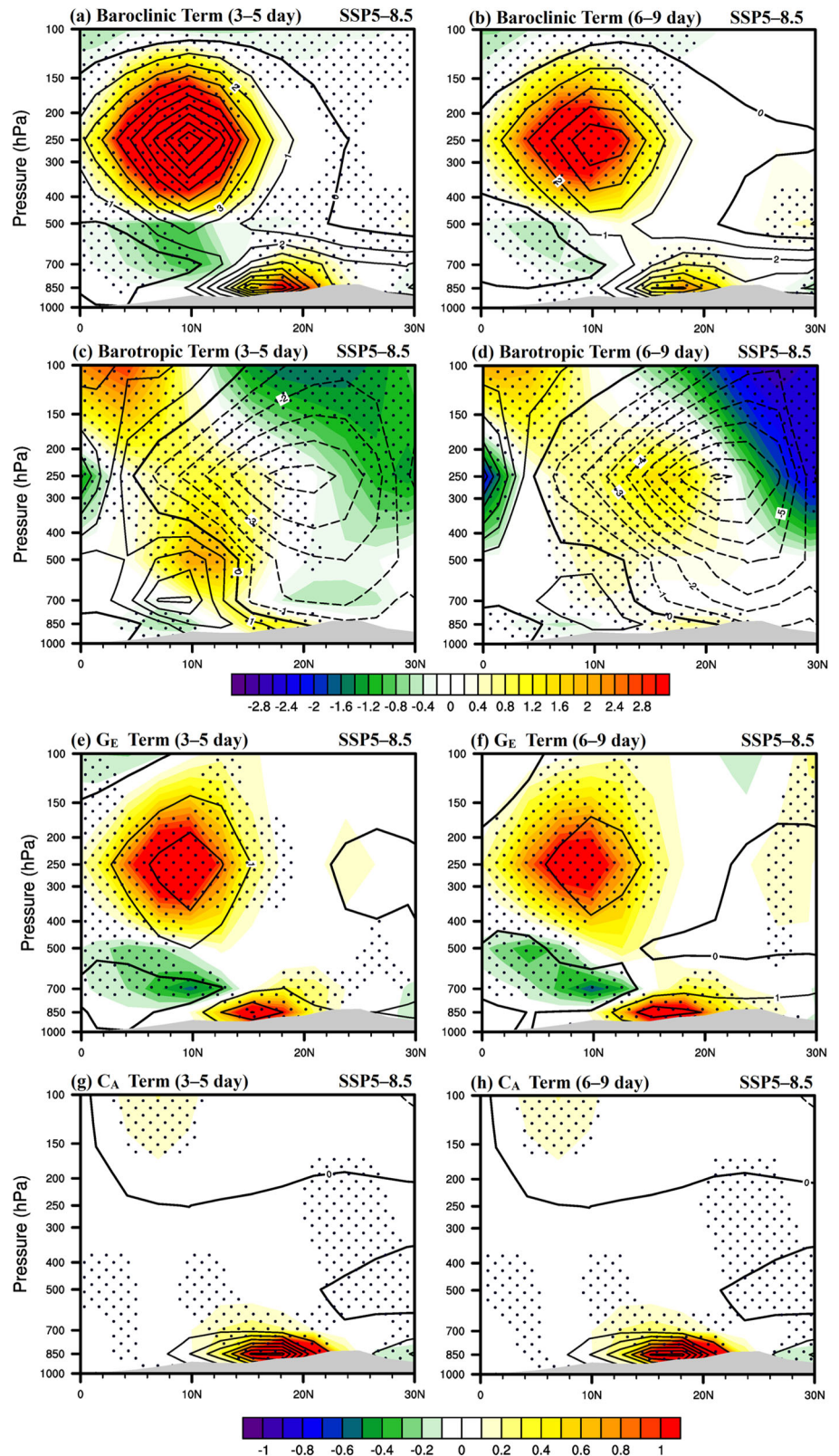
In general, we observe that warming in the Sahel-Sahara during the JJAS season at the end of the 21st century is notably greater than that in the Guinea Coast, with mean surface potential temperatures increasing by 5 °C to 6.6 °C (3.8 °C to 4.2 °C) north (south) of 15°N, as shown in Fig. 6a, e. This surface warming pattern, driven largely by both local and large-scale

processes, aligns with the projected amplification of the MTG, particularly over the Sahel-Sahara, thereby intensifying the ZAPE. In fact, a previous study^{33,68} has indicated that surface temperatures by the end of the 21st century over southern Europe and the Mediterranean would increase in response to enhanced mid-troposphere anticyclonic circulation, large-scale subsidence, and reduced precipitation. These changes are associated with robust increases in surface shortwave downwelling radiation over much of Europe, the Mediterranean Sea, and northern Africa (Fig. 6c, g), while the Sahara warms preferentially in response to an anomalous increase in surface longwave downwelling radiation (Fig. 6d, h). Furthermore, the robust increases in precipitation also minimize low-level warming across the central Sahel, further enhancing the contrast in temperature between the Sahara and southern regions (Fig. 6b, f). Based on these results, we argue that the increased MTG over West Africa is partly responsible for providing the necessary energy for stronger AEW development under global warming by intensifying the AEJ (Fig. 2).

Furthermore, barotropic energy conversion, $(-\overrightarrow{V}'_H \cdot (\overrightarrow{V}' \cdot \nabla) \overrightarrow{V}_H)$ is the secondary source of EKE, converting zonal kinetic energy into EKE. For 3–5-day AEWs in the present-day climatology, two primary regions of positive barotropic conversion are evident, spanning the upper and mid-to-lower troposphere (contours in Figs. 4c, d and S30c, d). The positive values in the upper troposphere, starting around 0°, are driven by the anticyclonic divergent flow from the ITCZ and the strong shear of the Tropical Easterly Jet (TEJ)⁶⁵. The second region is in the middle troposphere, centered around 9°N, south of the AEJ. This region is associated with EKE production due to AEWs. In other words, the barotropic energy conversion that maintains AEWs occurs primarily south of the AEJ, where mostly 3–5-day AEWs occur. Meanwhile, on the northern flank of the AEJ, around 16°N, the barotropic conversion exhibits lower values, which become negative farther north toward the Sahara. This asymmetry on either side of the AEJ leads to the tilting of AEW axes. These results are consistent for the 6–9-day AEWs, although with a lower magnitude.

For both the 3–5-day and 6–9-day AEWs, a significant area of EKE sink (i.e., negative barotropic conversion) is observed north of 18°N below 700 hPa and north of 8°N above 700 hPa. The negative values are notably larger for the 6–9-day AEWs. This sink is associated with the

Fig. 4 | Projected changes in energetic terms. Meridional height cross-sections of CMIP6 EnsMean change (shaded, $m^2 s^{-2} day^{-1}$) in the JJAS a, b baroclinic term (C_{pk}), c, d barotropic term (C_k), e, f diabatic heating term (G_E), and g, h conversion term (C_A) under SSP5–8.5, averaged between $20^\circ W$ and $10^\circ E$. Contours represent present-day mean. Mean change calculated between 2070–2099 and 1985–2014. The left panel shows 3–5-day AEWs and the right panel shows 6–9-day AEWs. Stippling indicates grid points where at least 70% of ensemble members agree on the sign of the change in EnsMean. Values under topography are masked with gray shading.



shear in the subtropical jet⁵⁴. Under future warming, we find a robust increase in the barotropic conversion term near the tropopause (shaded in Figs. 4c, d and S30c, d), extending from the upper to the lower troposphere, spanning from the equator at upper levels to around $20^\circ N$ in the lower troposphere. Notably, there are regions of isolated projected decreases below 700 hPa, around $4^\circ N$ to $10^\circ N$. More

pronounced decreases are projected at mid-to-upper levels north of $22^\circ N$, with this pattern extending southward at upper levels. These results are consistent for both the 3–5-day and 6–9 day-AEWs, though the intensity is greater for the former. This pattern is consistent under the SSP2–4.5 scenario, although the magnitude of change is much lower.

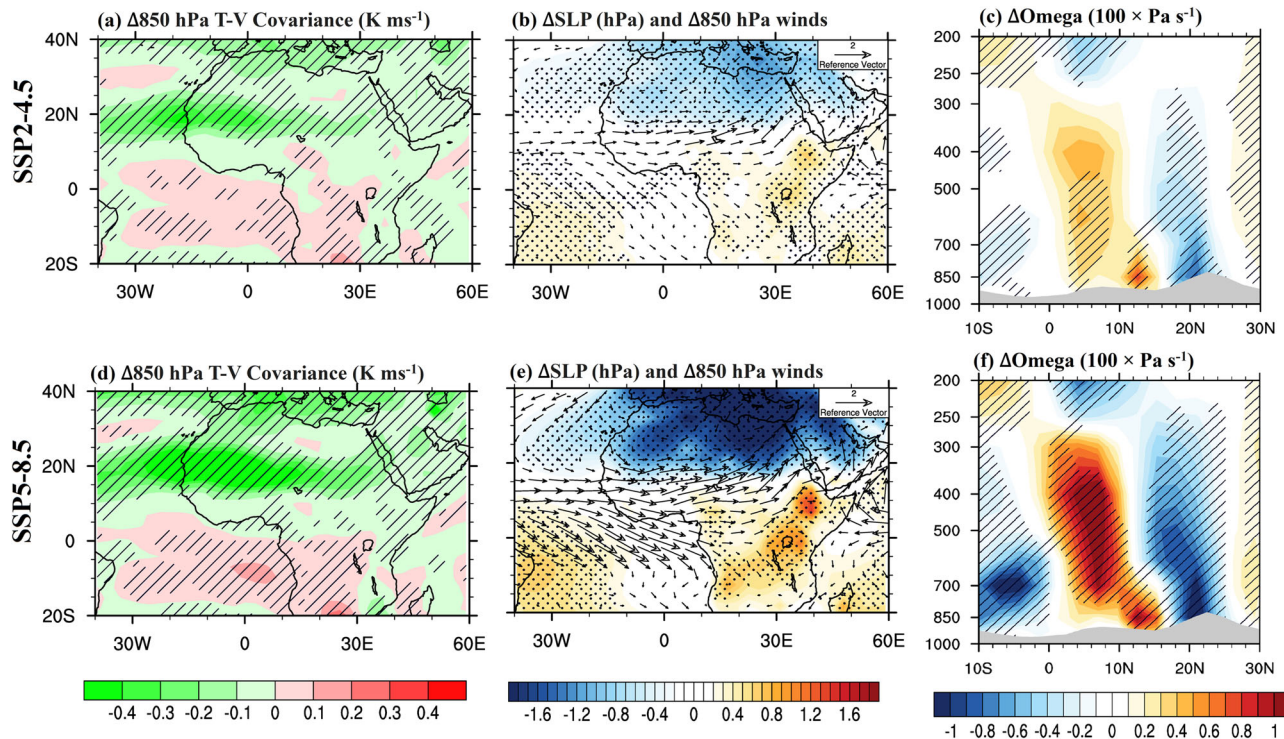


Fig. 5 | Projected changes in mean JJAS temperature–meridional wind covariance, sea level pressure and low-level wind, and vertical velocity. CMIP6 EnsMean change in JJAS **a, d** 3–5-day filtered temperature and meridional wind variance (t-v covariance) at 850 hPa, **b, e** sea level pressure and 850 hPa winds, and **c, f** vertical velocity. Mean change calculated between 2070–2099 and 1985–2014. Values under topography are masked with gray shading in (c, f). The mean vertical

velocity change in the latitude–height cross-section in (c) is averaged between 15°W and 15°E. Hatching indicates grid points where at least 70% of GCMs agree on the sign of the change in EnsMean. Areas with statistically significant differences at the 95% level are marked with black stippling in (b, e).

The next term in the energy cycle is the generation term ($G_E; \frac{\gamma}{T} \overline{Q_1 T'}$), representing the source of EAPE via diabatic heating, as shown in Figs. 4e, f and S30e, f. According to Michaelides⁶⁹, positive (negative) values of G_E indicate the generation (destruction) of EAPE, corresponding to the warming (cooling) of warm regions or the cooling (warming) of cold regions at the same latitude. The meridional distribution of the EnsMean G_E for both 3–5-day and 6–9-day AEWs is generally consistent, though the magnitude is higher for 3–5-day AEWs. This pattern of G_E , particularly in the upper troposphere, is similar to that of the baroclinic conversion term, suggesting that the EAPE consumed by baroclinic processes is partially offset by diabatic heating. For both 3–5-day and 6–9-day AEWs, two regions of positive G_E are observed in the present-day period (contours in Figs. 4e, f and S30e, f): one in the upper troposphere between 150 hPa and 500 hPa, centered around 8°N, and another below 700 hPa, near the core of the AEJ around 15°N. Under future warming (shaded areas in Figs. 4e, f and S30e, f), similar to the baroclinic conversion term, G_E in the mid-to-upper troposphere centered around 8°N and in the mid-to-lower troposphere centered around 15°N is projected to increase in the future for both types of AEWs under SSP5–8.5. Additionally, a region of projected decrease in G_E is evident between 500 hPa and 850 hPa south of 12°N. This pattern is consistent under the SSP2–4.5 scenario, although the magnitude of change is much lower.

The meridional cross-section of the conversion term ($C_A; -\frac{c_p \gamma}{T} \overline{V_H' T'} \cdot \nabla_H \overline{T}$), which represents the conversion of ZAPE to EAPE through eddy heat flux along the zonal mean temperature gradient, is shown in Figs. 4g, h and S30g, h. This conversion acts as an additional source of EAPE, complementing the baroclinic term. In the present-day period (see contour lines), unlike for the other terms, only one prominent region of conversion of ZAPE to EAPE (positive C_A) is observed for both 3–5-day and 6–9-day AEWs, extending from 8°N to 22°N in the mid-to-lower

troposphere. The magnitude of C_A in this region is comparable to that of G_E , suggesting a similar contribution to baroclinic conversion. This dominant contribution of C_A likely results from thermal advection (see Eq. 5 in Methods) associated with the large-scale MTG. Under future warming (see shaded areas in Figs. 4g, h and S30g, h), this region of EAPE generation intensifies and extends up to around 600 hPa. The intensification is comparable for both 3–5-day and 6–9-day AEWs, though the magnitude is significantly higher under the SSP5–8.5 scenario compared to SSP2–4.5.

Furthermore, our results show that in addition to the increase in ZAPE and the energetic terms, low-level heating over the region at the end of the 21st century leads to a deepening of the Saharan Heat Low (SHL), strengthening of the monsoon flow, and increased convergence along the ITCZ (Fig. 5). The enhanced SHL, along with warmer surface air temperatures, maintains the region’s low static stability. This low static stability facilitates greater interaction between surface temperature gradients and the potential vorticity gradients at the AEJ level, resulting in stronger low-level AEWs north of the AEJ^{4,64,70}. The pressure-driven increase in low-level westerly and southwesterly flow (Fig. 5b, e) yields greater convergence between the monsoon and Harmattan winds, leading to stronger vertical ascent along the intertropical discontinuity near 20°N over West Africa (Fig. 5c, f). We note that relative to ERA5, the CMIP6 models used herein accurately replicate a vertically deep region of ascent associated with the ITCZ near 8°N and a shallow region of ascent associated with the intertropical discontinuity near 17°N during the present-day period, indicating that the projected deepening of ascent near 20°N is not merely an amplification of model biases in simulating the large-scale overturning circulations in West Africa (Fig. S34). In fact, previous studies have shown that large-scale vertical ascent along the ITCZ contributes to the projected increases in AEW strength through vortex stretching^{35,40}. Furthermore, the increase in deep vertical ascent along the intertropical discontinuity at the end of the 21st century suggests the presence of increased latent heating

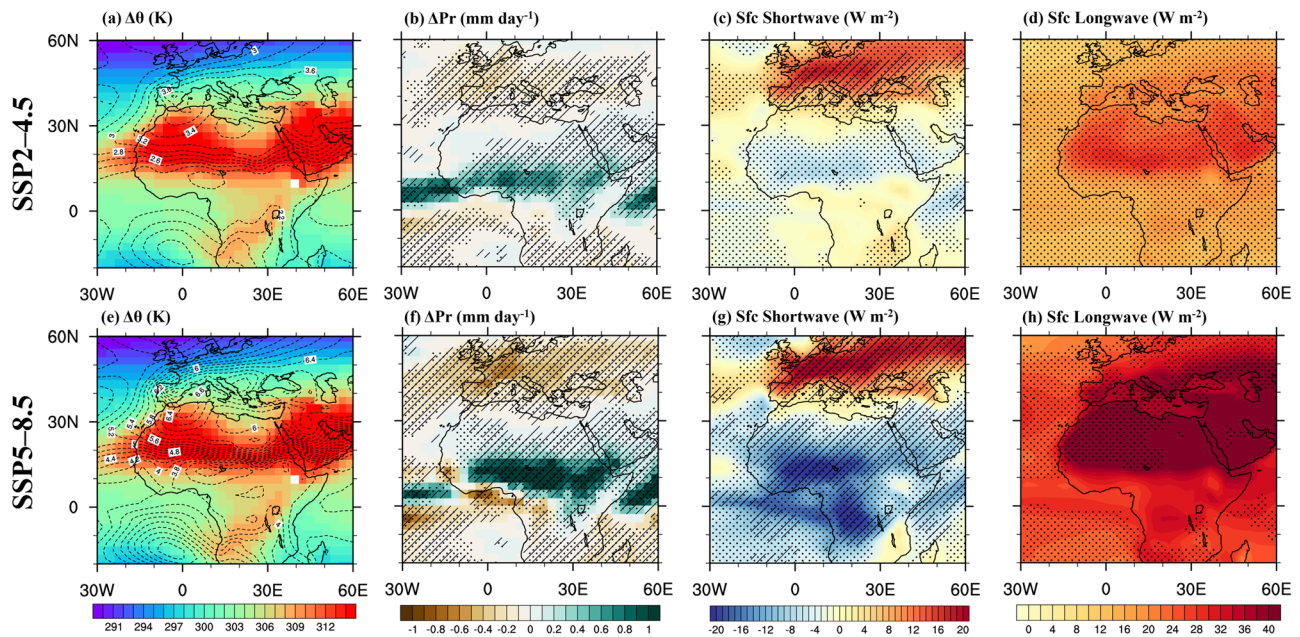


Fig. 6 | Projected changes in mean JJAS temperature, precipitation, and radiation. CMIP6 EnsMean change in JJAS **a, e** potential temperature (dashed lines), **b, f** precipitation, **c, g** surface downwelling shortwave radiation, and **d, h** surface downwelling longwave radiation under SSP2–4.5 (**a–d**) and SSP5–8.5 (**e–h**). Mean change calculated between 2070–2099 and 1985–2014. Shading in **b, f** represents the present-day mean JJAS potential temperature from CMIP6 EnsMean. Areas with

statistically significant differences at the 95% level are marked with black stippling, and hatching indicates grid points where at least 70% of ensemble members agree on the sign of the change in EnsMean. Hatching is deliberately removed from (**d, h**) because all models agree on the sign of the change in EnsMean.

(Fig. 5c, f). This increase in latent heating aligns with substantial increases in moist monsoon flow and precipitation across the Sahel (except for drying over the far western Sahel) (Figs. 6b, f and 5b, e).

While AEWs north of the AEJ typically exhibit dry dynamics in the current climate^{35,53}, the projected increase in moist convective processes in the Sahel implies an amplified role of such processes in AEW development along the Sahel-Saharan border in both SSP2–4.5 and SSP5–8.5. Given the significance of convectively driven diabatic heating in generating EAPE for AEW growth^{19,34}, it is possible that the increased moisture within and north of the AEJ region also plays a pivotal role in enhancing AEW energy. Consistent with the increased AEW activity, most CMIP6 models show a slight strengthening of the AEJ at the end of the 21st century (Fig. S35). While there is no consistent shift in the jet’s location across the CMIP6 models, nearly all models project increased low-level westerly flow beneath the AEJ, particularly on the jet’s poleward side (Fig. S35). This resultant enhancement in vertical zonal wind shear may bolster the growth of AEWs⁷¹, helping to elucidate the substantial increases in AEW activity that occur north of the AEJ core in response to elevated forcing (Fig. 2).

Overall, the combined dynamic and thermodynamic responses to the pattern of low-level warming create an environment conducive for stronger AEWs north of the AEJ core over West Africa. Indeed, nearly all CMIP6 models simulate an increase in the occurrence of intense (mean plus one standard deviation) and extremely intense (mean plus two standard deviations) AEWs along the Sahel-Saharan border (Fig. 7). This includes a median seasonal increase of about 20–40% for intense AEWs and 50–80% for extremely intense AEWs under both SSP2–4.5 and SSP5–8.5.

Discussion

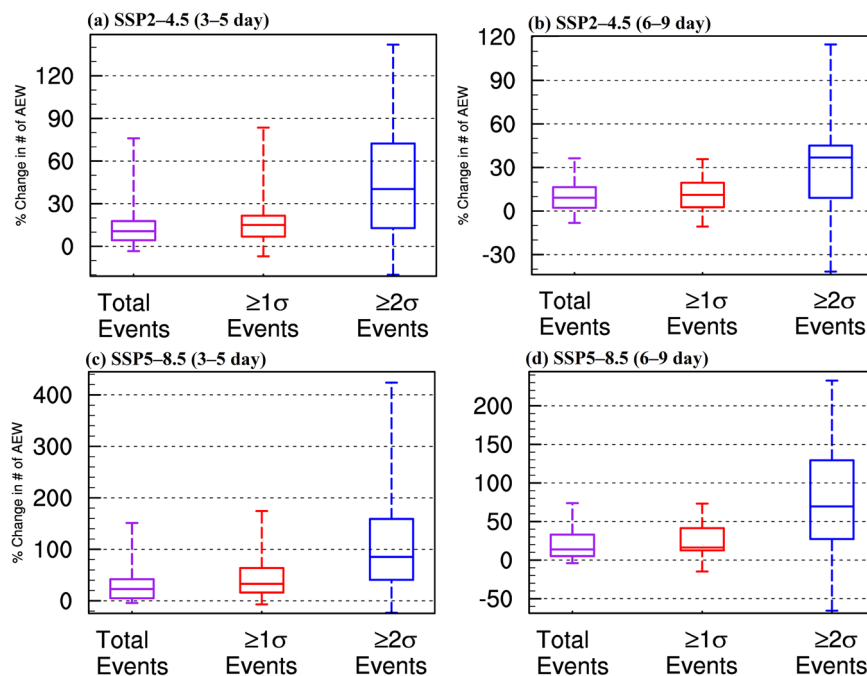
Previous studies have noted that AEWs exert significant influence on weather and climate by acting as precursor disturbances or preexisting cyclonic circulations for Atlantic tropical cyclone development, mobilizing and transporting Saharan dust within Africa and globally, and modulating rainfall across the Sahel during the West African monsoon. Hence, assessing how AEWs will change under continuous future warming is crucial for

understanding future weather patterns and associated impacts in the region. In this study, we use an ensemble of CMIP6 models to investigate how AEW activity will change under global warming as well as the environmental factors driving these changes. We use both MWV and EKE as proxies for AEW activity. Analyses are conducted separately for 3–5-day and 6–9-day AEWs, with changes assessed under the SSP2–4.5 and SSP5–8.5 scenarios.

While CMIP6 models exhibit variability in simulating AEW activity, EnsMean provides a reasonable representation of the spatial distribution of MWV and EKE associated with AEWs. Our results show that AEW activity in the Sahel-Saharan will intensify in the future, suggesting a strengthening of the northern AEW track. The lack of clear separation between the northern and southern tracks of 3–5-day AEWs and the presence of vertically deeper AEWs in specific subregions highlight the complexities and challenges in accurately capturing AEW characteristics in climate models. Additionally, we find no robust future changes in the region occupied by the southern AEW track in EnsMean, which may be attributed to uncertainty arising from the conflicting projections of individual models in this region.

We diagnose four energetic terms related to the generation of EKE and EAPE to identify the primary energy source responsible for the future intensification of AEW activity. Baroclinic energy conversion is the leading term for the maintenance of AEWs. The next two crucial terms are barotropic energy conversion and generation term (G_E) through diabatic heating. Our results indicate that under future warming, baroclinic conversion is the dominant source of future EKE for both types of AEWs, particularly near the tropopause. The projected increase in AEW activity is driven largely by an increase in ZAPE, resulting from stronger surface warming in the Sahel-Saharan region relative to the Guinea Coast (Fig. 6a, e). This uneven surface warming enhances the MTG, facilitating AEW growth via a stronger poleward baroclinic overturning process. Additionally, we find that barotropic conversion contributes to EKE generation primarily at the AEJ level, while energy generation due to diabatic heating is quantitatively similar, indicating that the G_E supplements the EAPE utilized by baroclinic conversion. Notably, both the baroclinic overturning process and G_E exhibit strong projected increases in the upper troposphere, suggesting enhanced latent heat release and convective heating in future climate scenarios. We

Fig. 7 | Projected change in percentage of intense and extreme intense AEWs. Boxplots of the change between 2070–2099 and 1985–2014 in the percentage of JJAS 3–5-day (a, c) and 6–9-day (b, d) AEWs that exceed the present-day period (1985–2014) one-SD and two-SD intensity thresholds at a reference location of (18°N, 0) under SSP2–4.5 (a, b) and SSP5–8.5 (c, d). Intensity thresholds are defined based on the magnitude of AEW meridional wind.



emphasize that low-level heating at the end of the 21st century will deepen the SHL and enhance the monsoon flow, resulting in stronger vertical ascent along the intertropical discontinuity (Fig. 5c, f). This leads to enhanced convective processes in the Sahel-Sahara, shown in previous studies to strengthen AEWs north of the AEJ through increased latent heating. The convectively driven latent heating is expected to enhance moisture transport into the region by enhancing the monsoon and, consequently, precipitation across the Sahel.

We note that the changing AEW activity under global warming could have substantial implications for the regional climate of the Sahelian region of West Africa. Given the link between AEWs and MCSs that cause extreme flooding in the Sahel, our results suggest an increase in the intensity and/or frequency of such events in a warmer climate. Additionally, the projected increase in AEW activity holds significant implications for future Saharan dust transport, given that the region with the highest projected increase in AEW activity lies over prolific dust sources within the western Sahara (Fig. 2). Strong winds associated with a northern-track AEW can transport dry Saharan air downstream, either inhibiting TC formation entirely or delaying tropical cyclogenesis until the wave reaches more favorable environmental conditions farther west in the Atlantic basin^{72,73}, where sea surface temperatures are warmer⁷⁴. Despite the increasing AEW activity, its impact on the tropical North Atlantic climate remains uncertain. The relationship between AEWs and TCs has been questioned, as recent studies suggest that suppressing AEWs does not substantially alter basin-wide seasonal Atlantic TC frequency but does influence TC intensity, genesis time, and location^{75,76}. These studies concluded that the presence or absence of AEWs could modulate the large-scale environment conducive for TC genesis, although there has been considerable evidence suggesting that northern-track waves can influence tropical cyclogenesis. Therefore, the potential future impact of the increased frequency of intense AEWs on TC development remains uncertain. Nonetheless, our findings highlight potential future changes in AEW activity, which could have significant implications for regional weather and climate variability, including changes in weather patterns, climate dynamics, and regional climate variability in West Africa. Some of the findings presented here are consistent with those of previous studies^{33,41} using CMIP5, emphasizing the robustness of AEW responses to future warming across successive generations of coupled climate models. Lastly, the analysis presented here focuses on the summer monsoon period (JJAS), which traditionally and climatologically coincides

with the peak months of AEW activity. However, a recent study⁷⁷ indicates that AEWs, along with other easterly waves, now occur year-round. To better capture the full spectrum of their impacts, future research should broaden its focus to include AEW activity beyond the traditional JJAS period.

Methods

In this study, we use climate simulations from the present day (1985–2014) and the end of the 21st century (2070–2099) from 24 CMIP6 models⁴⁸. For each model, we use the first realization ('r1i1p1f1') for the present-day and future projection periods. The future projection is based on two SSP, including an intermediate greenhouse gas (GHG) emission scenario (SSP2–4.5) and an extreme scenario with very high GHG emissions (SSP5–8.5). We select only models that deliver complete outputs for all meteorological variables used for all the analyses presented herein. For all variables, we investigate the response to future warming by comparing the present-day period in the historical simulation with projections for the end of the 21st century. We focus on the end of the century, where studies have shown that forced changes are relatively larger than internal variability.

To evaluate the accuracy of the CMIP6-simulated AEWs, we compare the model results with the fifth-generation European Centre for Medium-Range Weather Forecasts (ECMWF) atmospheric reanalysis (ERA5)⁷⁸ at a spatial resolution of $0.25^\circ \times 0.25^\circ$. Broad spatial assessment and several statistical metrics are used to evaluate the models, including percentage bias, NRMSE, PCC, and TSS, which have been used extensively in our previous studies (see Eqs. 1–4 in Akinsanola et al.⁵⁰). Furthermore, we employ the multimodel ensemble mean (referred to hereafter as EnsMean) to address systematic biases due to model differences^{50,79}. We regrid all datasets to the lowest model horizontal resolution ($2.81^\circ \times 2.81^\circ$) using an area-conserving remapping procedure, which is implemented in the Climate Data Operators (<https://code.zmaw.de/projects/cdo>) to produce EnsMean. Furthermore, following Akinsanola et al.⁵⁰, we estimate statistical robustness, particularly for analyses of spatial changes, by highlighting grid points where at least 70% of CMIP6 models agree on the sign of the change in EnsMean. In addition, a Student's *t*-test is used to identify the grid points where changes are statistically significant (at the 95% confidence level). We focus only on the monsoon period of June–July–August–September (JJAS), corresponding to the season when AEWs are active.

Tracking algorithm^{43,81,82}, MWV, and EKE approaches^{33,41,51,52} are the most common methods for detecting AEWs. Tracking algorithms, while effective, are highly sensitive to parameter tuning, require high temporal resolution (six-hourly or higher), demand substantial computational resources, and may overlook weaker AEWs^{17,52}. These limitations make tracking algorithms more suitable for single-model analysis, where such fine-tuning and resource allocation are more feasible. In contrast, the MWV and EKE approaches provide a more computationally efficient alternative and offer a clear, cohesive spatial representation of average AEW activity^{33,41,51-54,83}. These methods are better suited for analyzing long-term climate datasets and large model ensembles^{33,83}, making them more practical for the current study.

In this study, we use both the MWV and EKE methods. For the variance method, we detect AEWs using the meridional component of wind at 700 hPa and 850 hPa. We isolate variations in the flow associated with the passing of AEWs by band-pass filtering⁸⁴ the daily time series of the JJAS meridional wind (each year) to identify AEWs of 3–5-day and 6–9-day periods. Afterward, we compute the variance of the filtered time series at each grid point to attain a proxy of mean AEW activity. Furthermore, we identify the number of AEWs during JJAS by counting the instances in which the filtered daily mean meridional wind at the 850 hPa level exceeds 1 ms⁻¹. This counting is done at a reference point north of the EnsMean AEJ core in both the present-day and end-of-the-21st-century periods (18°N, 0°E; Fig. 1). We consider each instance a separate AEW event. In cases where the filtered meridional wind exceeds 1 ms⁻¹ on consecutive days, we consider only the day with the highest meridional wind value to prevent duplication of AEW events. To evaluate changes in the average number of intense AEWs, we calculate a distribution of AEW event intensities based on the 850 hPa meridional wind magnitude associated with each AEW at (18°N, 0°E) during the present-day period (i.e., 1985 to 2014). Following the approach of Skinner and Diffenbaugh³³, for each model, we define an AEW as intense if its meridional wind exceeds the mean-plus-one-standard-deviation threshold derived from the present-day period's distribution. From these, we designate an AEW as extremely intense if its meridional wind exceeds the mean-plus-two-standard-deviations threshold from the present-day period's distribution. Subsequently, we compute the percentage difference in the number of AEWs that exceed intensity thresholds in each model's present-day and end-of-the-21st-century periods.

Finally, the EKE is calculated as follows:

$$EKE = \frac{u'^2 + v'^2}{2} \quad (1)$$

where u and v represent the zonal and meridional winds, respectively. The primes indicate band-pass filtered anomalies of the daily wind field. We have filtered u and v for 3–5- and 6–9-day periods.

To better understand the factors contributing to changes in EKE, we employ the energetics analyses originally formulated by Lorenz⁶² for the general circulation of the atmosphere and later modified for a limited area^{63,65} by incorporating energy transport at the boundaries. AEWs can be regarded as eddy disturbances propagating along the zonal flow, with energy conversions classified into contributions from the zonal mean state and eddies⁶⁵. The primary source of energy for eddies is the available potential energy, which is subsequently converted into kinetic energy⁶². Both available potential and kinetic energy can be decomposed into their mean and eddy components. The generation of EKE in AEWs is driven primarily by baroclinic and barotropic energy conversions, as well as diabatic heating processes⁸⁵. These energy conversions are described by the Lorenz energy cycle, which governs the interaction between EKE (K_E) and available potential energy in an open system and can be expressed as follows:

$$\frac{\partial K_E}{\partial t} = C_k + C_{pk} - D_E + K_{EB} + \phi_{EB} \quad (2)$$

$$\frac{\partial A_E}{\partial t} = C_A - C_{pk} + G_E + A_{EB} \quad (3)$$

where K_E is the average EKE; A_E is the EAPE; and C_k is barotropic energy conversion, which captures the conversion of zonal to EKE through zonal (u) and meridional (v) wind shears. Also, C_{pk} represents the baroclinic energy conversion term, accounting for the conversion of A_E to K_E through vertical overturning. Note that the reappearance of this term with opposite sign in Eq. 3 indicates that the consumed A_E is converted to K_E , or vice versa. D_E represents the dissipation of energy due to friction, whereas K_{EB} and A_{EB} are the boundary fluxes of K_E and available potential energy, respectively, advecting into and out of the region of interest. ϕ_{EB} is the boundary pressure work done by the eddies.

The conversion term of ZAPE to A_E by means of the eddy heat flux along the zonal mean temperature gradient is given by C_A in Eq. 3. The generation of A_E by diabatic heating is given as G_E . A positive value of G_E (generation of A_E) results from heating in warmer regions or cooling in colder regions at the same latitude⁶⁹. In contrast, a negative value of G_E (destruction of A_E) is due to cooling in warmer regions or heating in colder regions at the same latitude.

The energy conversion terms are calculated as

$$C_k = -\overrightarrow{V'_H} \cdot (\overrightarrow{V}' \cdot \nabla) \overrightarrow{V}_H \quad (4)$$

$$C_{pk} = -\frac{R}{p} \overline{\omega' T'} \quad (5)$$

$$C_A = -\frac{c_p \gamma}{T} \overrightarrow{V'_H} T' \cdot \nabla_H \bar{T} \quad (6)$$

$$G_E = \frac{\gamma}{T} \overline{Q_1 T'} \quad (7)$$

where T denotes temperature, $\omega = \frac{\partial p}{\partial t}$ is vertical velocity, V_H is horizontal wind speed, and p is pressure. Also, for $\gamma = \frac{\Gamma_d}{\Gamma_d - \Gamma}$, Γ_d and Γ are the dry adiabatic and observed lapse rates, respectively; C_p is the heat capacity at constant pressure; R is the dry air gas constant; and Q_1 is the apparent heat source.

The apparent heat source is calculated as:

$$Q_1 = \frac{c_p T}{\theta} \left(\frac{\partial \theta}{\partial t} + u \frac{\partial \theta}{\partial \phi} + v \frac{\partial \theta}{\partial \lambda} + \omega \frac{\partial \theta}{\partial p} \right) \quad (8)$$

where θ is the potential temperature, and u and v are zonal and meridional velocities. Primes in these equations are calculated using the two band-pass filters. Following Hsieh and Cook⁶⁵, higher-order terms (i.e., those involving triple products of perturbations) in Eqs. 1 and 2 are neglected in the computation. The positive and negative values in these figures represent gain and loss of EKE or EAPE, respectively.

Data availability

All datasets used in this study are publicly and freely available. CMIP6 data are publicly available through the Earth System Grid Federation at <http://esgf.llnl.gov/>. The ERA5 reanalysis dataset is produced by the Copernicus Climate Change Service at the European Centre for Medium-Range Weather Forecasts (ECMWF) and is available at <https://www.ecmwf.int/en/forecasts/dataset/ecmwf-reanalysis-v5>.

Code availability

All analyses and figures were computed and drawn using NCAR Command Language (<https://www.ncl.ucar.edu/>) and Python (<https://www.python.org/>). The code used for the analysis in this study is available upon request from the corresponding author.

Received: 29 April 2024; Accepted: 19 December 2024;

Published online: 02 January 2025

References

- Burpee, R. W. The origin and structure of easterly waves in the lower troposphere of North Africa. *J. Atmos. Sci.* **29**, 77–90 (1972).
- Reed, R. J., Norquist, D. C. & Recker, E. E. The structure and properties of African wave disturbances as observed during phase III of GATE. *Mon. Weather Rev.* **105**, 317–333 (1977).
- Charney, J. G. & Stern, M. E. On the stability of internal baroclinic jets in a rotating atmosphere. *J. Atmos. Sci.* **19**, 159–172 (1962).
- Pytharoulis, I. & Thorncroft, C. The low-level structure of African easterly waves in 1995. *Mon. Weather Rev.* **127**, 2266–2280 (1999).
- Schubert, W. H., Ciesielski, P. E., Stevens, D. E. & Kuo, H.-C. Potential vorticity modeling of the ITCZ and the Hadley circulation. *J. Atmos. Sci.* **48**, 1493–1509 (1991).
- Hsieh, J.-S. & Cook, K. H. Generation of African easterly wave disturbances: relationship to the African easterly jet. *Mon. Weather Rev.* **133**, 1311–1327 (2005).
- Mekonnen, A., Thorncroft, C. D. & Aiyyer, A. R. Analysis of convection and its association with African easterly waves. *J. Clim.* **19**, 5405–5421 (2006).
- Kiladis, G. N., Thorncroft, C. D. & Hall, N. M. J. Three-dimensional structure and dynamics of African easterly waves. Part I: observations. *J. Atmos. Sci.* **63**, 2212–2230 (2006).
- Berry, G. J. & Thorncroft, C. Case study of an intense African easterly wave. *Mon. Weather Rev.* **133**, 752–766 (2005).
- Hsieh, J.-S. & Cook, K. H. On the instability of the African easterly jet and the generation of African waves: reversals of the potential vorticity gradient. *J. Atmos. Sci.* **65**, 2130–2151 (2008).
- Russell, J. O. H. & Aiyyer, A. The potential vorticity structure and dynamics of African easterly waves. *J. Atmos. Sci.* **77**, 871–890 (2020).
- Russell, J. O. H., Aiyyer, A. & Dylan White, J. African easterly wave dynamics in convection-permitting simulations: Rotational stratiform instability as a conceptual model. *J. Adv. Model. Earth Syst.* **12**, e2019MS001706 (2020).
- Grogan, D. F. P., Nathan, T. R. & Chen, S.-H. Effects of Saharan dust on the linear dynamics of African easterly waves. *J. Atmos. Sci.* **73**, 891–911 (2016).
- Bercos-Hickey, E., Nathan, T. R. & Chen, S.-H. Saharan dust and the African easterly jet–African easterly wave system: structure, location and energetics. *Q. J. R. Meteorol. Soc.* **143**, 2797–2808 (2017).
- Nathan, T. R., Grogan, D. F. P. & Chen, S.-H. Subcritical destabilization of African easterly waves by Saharan mineral dust. *J. Atmos. Sci.* **74**, 1039–1055 (2017).
- Thorncroft, C. & Hodges, K. African easterly wave variability and its relationship to Atlantic tropical cyclone activity. *J. Clim.* **14**, 1166–1179 (2001).
- Landsea, C. W. & Gray, W. M. The strong association between western Sahelian monsoon rainfall and intense Atlantic hurricanes. *J. Clim.* **5**, 435–453 (1992).
- Pasch, R. J. & Avila, L. A. Atlantic tropical systems of 1992. *Mon. Weather Rev.* **122**, 539–548 (1994).
- Fink, A. H. & Reiner, A. Spatiotemporal variability of the relation between African Easterly Waves and West African Squall Lines in 1998 and 1999. *J. Geophys. Res.* **108**, 4332 (2003).
- Thorncroft, C. D., Hall, N. M. J. & Kiladis, G. N. Three-dimensional structure and dynamics of African easterly waves. Part III: Genesis. *J. Atmos. Sci.* **65**, 3596–3607 (2008).
- Berry, G. J. & Thorncroft, C. D. African easterly wave dynamics in a mesoscale numerical model: the upscale role of convection. *J. Atmos. Sci.* **69**, 1267–1283 (2012).
- Meteorology of Tropical West Africa: The Forecasters' Handbook* (eds Parker, D. J. & Diop-Kane, M.) (John Wiley & Sons, Nashville, TN) <https://onlinelibrary.wiley.com/doi/book/10.1002/9781118391297> (2017).
- Dandoy, S. et al. Atlantic hurricane response to Saharan greening and reduced dust emissions during the mid-Holocene. *Clim. Past* **17**, 675–701 (2021).
- Bian, J., Räisänen, J. & Zhang, Q. Mechanisms for African easterly wave changes in simulations of the mid-Holocene. *Clim. Dyn.* **61**, 3165–3178 (2023).
- Chen, T.-C. Characteristics of African easterly waves depicted by ECMWF reanalyses for 1991–2000. *Mon. Weather Rev.* **134**, 3539–3566 (2006).
- Wu, M.-L. C., Reale, O. & Schubert, S. D. A characterization of African easterly waves on 2.5–6-day and 6–9-day time scales. *J. Clim.* **26**, 6750–6774 (2013).
- De Felice, P., Monkam, D., Viltard, A. & Ouss, C. Characteristics of North African 6–9 Day Waves during Summer 1981. *Mon. Weather Rev.* **118**, 2624–2633 (1990).
- Crétat, J., Vizi, E. K. & Cook, K. H. The relationship between African easterly waves and daily rainfall over West Africa: observations and regional climate simulations. *Clim. Dyn.* **44**, 385–404 (2015).
- Diedhiou, A., Janicot, S., Viltard, A. & De Felice, P. Evidence of two regimes of easterly waves over West Africa and the tropical Atlantic. *Geophys. Res. Lett.* **25**, 2805–2808 (1998).
- Diedhiou, A., Janicot, S., Viltard, A., de Felice, P. & Laurent, H. Easterly wave regimes and associated convection over West Africa and tropical Atlantic: results from the NCEP/NCAR and ECMWF reanalyses. *Clim. Dyn.* **15**, 795–822 (1999).
- Viltard, A., de Felice, P. & Oubuih, J. Comparison of the African and the 6–9 day wave-like disturbance patterns over West-Africa and the tropical Atlantic during summer 1985. *Meteorol. Atmos. Phys.* **62**, 91–99 (1997).
- Cornforth, R. J., Hoskins, B. J. & Thorncroft, C. D. The impact of moist processes on the African easterly jet–African easterly wave system. *Q. J. R. Meteorol. Soc.* **135**, 894–913 (2009).
- Skinner, C. B. & Diffenbaugh, N. S. Projected changes in African easterly wave intensity and track in response to greenhouse forcing. *Proc. Natl. Acad. Sci. USA* **111**, 6882–6887 (2014).
- Goldenberg, S. B. & Shapiro, L. J. Physical mechanisms for the association of El Niño and West African rainfall with Atlantic major hurricane activity. *J. Clim.* **9**, 1169–1187 (1996).
- Lau, K.-H. & Lau, N.-C. The energetics and propagation dynamics of tropical summertime synoptic-scale disturbances. *Mon. Weather Rev.* **120**, 2523–2539 (1992).
- Gu, G., Adler, R. F., Huffman, G. J. & Curtis, S. African easterly waves and their association with precipitation. *J. Geophys. Res.* **109**, D04101 (2004).
- Knippertz, P. & Todd, M. C. The central west Saharan dust hot spot and its relation to African easterly waves and extratropical disturbances. *J. Geophys. Res.* **115**, 2009JD012819 (2010).
- Ross, R. S. & Krishnamurti, T. N. Low-level African easterly wave activity and its relation to Atlantic tropical cyclogenesis in 2001. *Mon. Weather Rev.* **135**, 3950–3964 (2007).
- Hankes, I., Wang, Z., Zhang, G. & Fritz, C. Merger of African easterly waves and formation of Cape Verde storms. *Q. J. R. Meteorol. Soc.* **141**, 1306–1319 (2015).
- Chen, S.-H. & Liu, Y.-C. The relation between dry vortex merger and tropical cyclone genesis over the Atlantic Ocean: D-Vortex merger and Atlantic TC genesis. *J. Geophys. Res.* **119**, 11,641–11,661 (2014).
- Martin, E. R. & Thorncroft, C. Representation of African easterly waves in CMIP5 models. *J. Clim.* **28**, 7702–7715 (2015).
- Hannah, W. M. & Aiyyer, A. Reduced African easterly wave activity with quadrupled CO₂ in the superparameterized CESM. *J. Clim.* **30**, 8253–8274 (2017).

43. Brannan, A. L. & Martin, E. R. Future characteristics of African Easterly Wave tracks. *Clim. Dyn.* **52**, 5567–5584 (2019).
44. Kebe, I., Diallo, I., Sylla, M. B., De Sales, F. & Diedhiou, A. Late 21st century projected changes in the relationship between precipitation, African Easterly Jet, and African Easterly Waves. *Atmosphere* **11**, 353 (2020).
45. Bercos-Hickey, E. & Patricola, C. M. Anthropogenic influences on the African easterly jet–African easterly wave system. *Clim. Dyn.* **57**, 2779–2792 (2021).
46. Sun, Q., Miao, C. & Duan, Q. Comparative analysis of CMIP3 and CMIP5 global climate models for simulating the daily mean, maximum, and minimum temperatures and daily precipitation over China. *J. Geophys. Res.* **120**, 4806–4824 (2015).
47. Koutroulis, A. G., Grillakis, M. G., Tsanis, I. K. & Papadimitriou, L. Evaluation of precipitation and temperature simulation performance of the CMIP3 and CMIP5 historical experiments. *Clim. Dyn.* **47**, 1881–1898 (2016).
48. Eyring, V. et al. Overview of the Coupled Model Intercomparison Project Phase 6 (CMIP6) experimental design and organization. *Geosci. Model Dev.* **9**, 1937–1958 (2016).
49. Akinsanola, A. A., Kooperman, G. J., Pendergrass, A. G., Hannah, W. M. & Reed, K. A. Seasonal representation of extreme precipitation indices over the United States in CMIP6 present-day simulations. *Environ. Res. Lett.* **15**, 094003 (2020).
50. Akinsanola, A. A., Chen, Z., Kooperman, G. J. & Bobde, V. Robust future intensification of winter precipitation over the United States. *npj Clim Atmos Sci* **7**, 1–11 (2024).
51. Russell, J. O., Aiyyer, A., White, J. D. & Hannah, W. Revisiting the connection between African Easterly Waves and Atlantic tropical cyclogenesis. *Geophys. Res. Lett.* **44**, 587–595 (2017).
52. Bercos-Hickey, E., Patricola, C. M., Loring, B. & Collins, W. D. The relationship between African easterly waves and tropical cyclones in historical and future climates in the HighResMIP-PRIMAVERA simulations. *JGR Atmos.* **128**, e2022JD037471 (2023).
53. Raj, J., Bangalath, H. K. & Stenchikov, G. Future projection of the African easterly waves in a high-resolution atmospheric general circulation model. *Clim. Dyn.* **61**, 3081–3102 (2023).
54. Bangalath, H. K., Raj, J. & Stenchikov, G. Sensitivity of African easterly waves to dust forcing. *JGR Atmos.* **128**, e2023JD038656 (2023).
55. Akinsanola, A. A. & Zhou, W. Ensemble-based CMIP5 simulations of West African summer monsoon rainfall: current climate and future changes. *Theor. Appl. Climatol.* **136**, 1021–1031 (2019).
56. Adeyeri, O. E. et al. The trend and spatial spread of multisectoral climate extremes in CMIP6 models. *Sci. Rep.* **12**, 21000 (2022).
57. Di Virgilio, G. et al. Selecting CMIP6 GCMs for CORDEX dynamical downscaling: model performance, independence, and climate change signals. *Earth's Future* **10**, e2021EF002625 (2022).
58. Alexander, L. V. & Arblaster, J. M. Historical and projected trends in temperature and precipitation extremes in Australia in observations and CMIP5. *Weather Clim. Extrem.* **15**, 34–56 (2017).
59. Knippertz, P., Fink, A. H., Reiner, A. & Speth, P. Three late summer/early autumn cases of tropical–extratropical interactions causing precipitation in Northwest Africa. *Mon. Weather Rev.* **131**, 116–135 (2003).
60. Knippertz, P. Tropical–extratropical interactions related to upper-level troughs at low latitudes. *Dyn. Atmos. Oceans* **43**, 36–62 (2007).
61. Chang, E. K. M., Guo, Y. & Xia, X. CMIP5 multimodel ensemble projection of storm track change under global warming. *J. Geophys. Res.* **117**, D23118 (2012).
62. Lorenz, E. N. Available potential energy and the maintenance of the general circulation. *Tellus* **7**, 157–167 (1955).
63. Norquist, D. C., Recker, E. E. & Reed, R. J. The energetics of African wave disturbances as observed during phase III of GATE. *Mon. Weather Rev.* **105**, 334–342 (1977).
64. Thorncroft, C. D. An idealized study of African easterly waves. III: more realistic basic states. *Q. J. R. Meteorol. Soc.* **121**, 1589–1614 (1995).
65. Hsieh, J.-S. & Cook, K. H. A study of the energetics of African easterly waves using a regional climate model. *J. Atmos. Sci.* **64**, 421–440 (2007).
66. Cook, K. H. Generation of the African easterly jet and its role in determining West African precipitation. *J. Clim.* **12**, 1165–1184 (1999).
67. Grist, J. P. & Nicholson, S. E. A study of the dynamic factors influencing the rainfall variability in the West African Sahel. *J. Clim.* **14**, 1337–1359 (2001).
68. Giorgi, F. & Lionello, P. Climate change projections for the Mediterranean region. *Glob. Planet. Change* **63**, 90–104 (2008).
69. Michaelides, S. C. A spatial and temporal energetics analysis of a baroclinic disturbance in the Mediterranean. *Mon. Weather Rev.* **120**, 1224–1243 (1992).
70. Chang, C.-B. Impact of desert environment on the genesis of African wave disturbances. *J. Atmos. Sci.* **50**, 2137–2145 (1993).
71. Leroux, S. & Hall, N. M. J. On the relationship between African easterly waves and the African easterly jet. *J. Atmos. Sci.* **66**, 2303–2316 (2009).
72. Hopsch, S. B., Thorncroft, C. D. & Tyle, K. R. Analysis of African easterly wave structures and their role in influencing tropical cyclogenesis. *Mon. Weather Rev.* **138**, 1399–1419 (2010).
73. Chen, T.-C., Wang, S.-Y. & Clark, A. J. North Atlantic hurricanes contributed by African easterly waves north and south of the African easterly jet. *J. Clim.* **21**, 6767–6776 (2008).
74. Crespo, L. R., Keenlyside, N. & Koseki, S. The role of sea surface temperature in the atmospheric seasonal cycle of the equatorial Atlantic. *Clim. Dyn.* **52**, 5927–5946 (2019).
75. Danso, D. K., Patricola, C. M. & Bercos-Hickey, E. Influence of African easterly wave suppression on Atlantic tropical cyclone activity in a convection-permitting model. *Geophys. Res. Lett.* **49**, e2022GL100590 (2022).
76. Patricola, C. M., Saravanan, R. & Chang, P. The response of Atlantic tropical cyclones to suppression of African easterly waves. *Geophys. Res. Lett.* **45**, 471–479 (2018).
77. Hollis, M. A. et al. A global climatology of tropical easterly waves. *Clim. Dyn.* **62**, 2317–2332 (2024).
78. Hersbach, H. et al. The ERA5 global reanalysis. *Q. J. R. Meteorol. Soc.* **146**, 1999–2049 (2020).
79. Akinsanola, A. A. & Zhou, W. Projection of West African summer monsoon rainfall in dynamically downscaled CMIP5 models. *Clim. Dyn.* **53**, 81–95 (2019).
80. Akinsanola, A. A., Kooperman, G. J., Reed, K. A., Pendergrass, A. G. & Hannah, W. M. Projected changes in seasonal precipitation extremes over the United States in CMIP6 simulations. *Environ. Res. Lett.* **15**, 104078 (2020).
81. Bain, C. L., Williams, K. D., Milton, S. F. & Heming, J. T. Objective tracking of African Easterly Waves in Met Office models. *Q. J. R. Meteorol. Soc.* **140**, 47–57 (2014).
82. Brammer, A. & Thorncroft, C. D. Variability and evolution of African easterly wave structures and their relationship with tropical cyclogenesis over the Eastern Atlantic. *Mon. Weather Rev.* **143**, 4975–4995 (2015).
83. Skinner, C. B. & Diffenbaugh, N. S. The contribution of African easterly waves to monsoon precipitation in the CMIP3 ensemble. *J. Geophys. Res.* **118**, 3590–3609 (2013).
84. Duchon, C. E. Lanczos filtering in one and two dimensions. *J. Appl. Meteorol.* **18**, 1016–1022 (1979).
85. McCrary, R. R., Randall, D. A. & Stan, C. Simulations of the West African monsoon with a superparameterized climate model. Part II: African easterly waves. *Journal of Climate* **27**, 8323–8341 (2014).

Acknowledgements

We appreciate the World Climate Research Programme's (WCRP) working group on coupled modeling, which is responsible for the CMIP6 models. The authors acknowledge the climate modeling groups listed in Table S1 for producing and making their model outputs available, and the ESGF for archiving the model outputs and providing access. We are also grateful to the services that have operated the ERA5 dataset.

Author contributions

Akintomide A. Akinsanola: Conceptualization, methodology, data analysis, visualization, writing—original draft preparation, Writing—review and editing. Vishal Bobde and Adeyemi A. Adebiyi: Data analysis, visualization, and writing—review and editing. Oluwafemi E. Adeyeri, Alain T. Tamoffo, and Derrick K. Danso: Writing—review and editing. All authors discussed the study results and reviewed the manuscript.

Competing interests

Akintomide A. Akinsanola is an Editorial Board Member for *Communications Earth & Environment*, but was not involved in the editorial review of, nor the decision to publish this article. All other authors declare no competing interests.

Additional information

Supplementary information The online version contains supplementary material available at <https://doi.org/10.1038/s43247-024-01981-9>.

Correspondence and requests for materials should be addressed to Akintomide A. Akinsanola.

Peer review information *Communications Earth & Environment* thanks Shun-Nan Wu and the other, anonymous, reviewer(s) for their contribution to the peer review of this work. Primary Handling Editor: Alireza Bahadori. A peer review file is available.

Reprints and permissions information is available at <http://www.nature.com/reprints>

Publisher's note Springer Nature remains neutral with regard to jurisdictional claims in published maps and institutional affiliations.

Open Access This article is licensed under a Creative Commons Attribution 4.0 International License, which permits use, sharing, adaptation, distribution and reproduction in any medium or format, as long as you give appropriate credit to the original author(s) and the source, provide a link to the Creative Commons licence, and indicate if changes were made. The images or other third party material in this article are included in the article's Creative Commons licence, unless indicated otherwise in a credit line to the material. If material is not included in the article's Creative Commons licence and your intended use is not permitted by statutory regulation or exceeds the permitted use, you will need to obtain permission directly from the copyright holder. To view a copy of this licence, visit <http://creativecommons.org/licenses/by/4.0/>.

© The Author(s) 2025